Research Article | Vol. 33, No. 13 / 30 Jun 2025 / Optics Express 28467
Optics EXPRESS

Numerical realization of tunable triple-band slow wave and bidirectional rainbow trapping in magneto-optical heterostructures

MENGTING YANG,[1,†] YUN YOU,[2,†] YAMEI LUO,[1] KANGLE YONG,[1] DELONG FENG,[1] QIAN SHEN,[3,4] AND JIE XU[1,5]

[1]School of Medical Information and Engineering, Southwest Medical University, Luzhou 646000, China
[2]School of Science, East China Jiaotong University, Nanchang 330013, China
[3]School of Electronic Information Engineering, China West Normal University, Nanchong 637009, China
[4]qianshen913@cwnu.edu.cn
[5]xujie011451@163.com
[†]These authors contributed equally to this work

Abstract: Flexible energy storage and retrieval have long garnered significant attention as key research directions in modern science and technology. In recent decades, the realization of slow light/wave propagation and rainbow trapping/releasing using novel materials or mechanisms—such as metamaterials and metasurfaces—has emerged as a major research focus. However, existing slow-wave and rainbow-trapping structures—including those based on photonic crystals—suffer from key limitations: (1) structural complexity, (2) limited tunability, and (3) confinement to a single slow-wave band. Here, we propose, for what we believe is the first time, a bidirectional rainbow trapping and releasing (RTR) mechanism supported by three distinct and tunable slow-wave bands in magneto-optical heterostructures. By precisely tuning external magnetic fields or material parameters, we achieve dynamic control over slow-wave peaks, enabling tunable RTR band engineering. Furthermore, under a constant external magnetic field, we design a tapered magneto-optical heterostructure that serves as a high-sensitivity sensor for detecting the relative permittivity of dielectric media. The proposed tunable structure, featuring three slow-wave peak dispersions for bidirectional rainbow manipulation, along with the dielectric sensing platform, demonstrates strong potential for applications in physical/biological detection, high-efficiency optical communication, and advanced energy storage.

1. Introduction

Since ancient times, scientists have been intrigued by the control of light [1]. With technological advancement, light manipulation has become increasingly precise. However, Einstein's theory of special relativity states that, regardless of technological progress, the speed of light or electromagnetic (EM) waves can never reach zero in any system. This raises a fundamental question: to what extent can light/EM waves be slowed down? In recent years, significant progress has been made in slowing the propagation of light and EM waves [2,3]. In a Bose–Einstein condensate (BEC), the speed of light has been reduced to 17 m/s at extremely low temperatures [4]. Electromagnetically induced transparency (EIT) is another widely used mechanism to slow light [5–7]. However, BEC- or EIT-based slow waves are inherently limited by stringent experimental conditions or narrow operating bandwidths [8]. For EM waves, it is well established that the group velocity v_g (= $d\omega/dk$) can be engineered to approach zero, thereby realizing slow-wave propagation. Efficient approaches include the use of (1) left-handed metamaterials [9,10], (2) resonators [11–13], and (3) (topological) photonic crystals (PhCs) [14–17]. Topological slow light/wave has become a research hotspot in recent years due to its robustness against defects and

#568047 https://doi.org/10.1364/OE.568047
Journal © 2025 Received 15 May 2025; revised 16 Jun 2025; accepted 16 Jun 2025; published 26 Jun 2025

Optics EXPRESS

backscattering. Moreover, the group index n_g (= $c(dk/d\omega)$) [8] can be tuned from tens [18] to even hundreds [19] by adjusting the parameters of PhC unit cells.

Slow waves are widely used in various fields such as nonlinear enhancement [20], optical buffering, and sensing [21]. Rainbow trapping, where waves of different frequencies are trapped at different locations, is another intriguing phenomenon enabled by slow waves [22,23], and is particularly relevant for energy harvesting. Rainbow trapping and/or releasing (RTR) can also be achieved in PhCs [24]. Metamaterials and metasurfaces have been among the major research hotspots in the optics and photonics fields over the past decades. Novel phenomena such as multi-band filters [25], multi-band EIT [26], high-efficiency wireless communication [27–29], and near-field focusing [30] have been reported with the development of metamaterial and metasurface technologies. It has also been reported that metasurfaces can be used to achieve slow-wave propagation [31,32]. However, achieving tunable RTR in simple structures remains a significant challenge. Magneto-optical (MO) heterostructures provide a promising platform to achieve this goal. Similar to unidirectional edge states in topological PhCs, nonreciprocal surface magnetoplasmons (SMPs) at the interface of MO heterostructures composed of gyromagnetic materials such as yttrium iron garnet (YIG) also exhibit strong immunity to backscattering [33,34]. Compared to PhCs or metamaterials/metasurfaces, the propagation characteristics and dispersion relations can be readily tuned by adjusting the external magnetic field (EMF). Recently, we have reported several types of slow-wave heterostructures, with [35] or without [36] metamaterials, and demonstrated RTR in these structures. However, robust multi-band slow-wave propagation over a relatively broad bandwidth—crucial for parallel optical communication and computation—remains a challenge in both our prior works [35,36] and that of others, and is the central focus of this study.

In this work, we design and propose a novel layered MO heterostructure composed of air and YIG layers to achieve triple-band slow-wave propagation and RTR in the microwave regime. Note that YIG is a widely used MO mateiral, and it is selected in this work due to its low magnetic damping [37,38] and mature manufacturing process. Three slow-wave peaks with near-zero v_g, indicating extremely large n_g, are identified in the dispersion diagram of the surface modes. The theoretical relationship between the three slow-wave peaks and the EMF is investigated. Next, we design a simple straight MO heterostructure with a linearly varying EMF, either increasing or decreasing depending on the type of slow wave. Triple-band rainbow trapping is observed in this structure using finite-element-method (FEM) simulations. Moreover, the peak frequencies of the slow-wave modes are affected by both the air and YIG layer thicknesses. Therefore, by adjusting the air layer thicknesses, the trapped EM waves can be easily released. To achieve RTR under a uniform EMF, we further design a tapered MO heterostructure with a tapered YIG layer. A promising application—dielectric sensing—is also demonstrated using a tapered MO heterostructure with tapered air layers. The proposed tunable triple-band slow-wave and RTR system offers a novel route for high-performance all-optical communication and sensing, among other applications.

2. Triple-band slow waves in straight MO heterostructures

To achieve novel multiple-band effects, such as triple-band slow-wave propagation, the key is to design tailored dispersion diagrams for different types of slow waves. Here, we propose a five-layer configuration. As shown in Fig. 1(a), the structure consists of two metal layers acting as perfect electric conductor (PEC) boundaries, two adjacent air layers, and a central layer of magnetized YIG. Due to the applied external magnetic field, the air–YIG interfaces support two oppositely propagating one-way SMPs induced by broken time-reversal symmetry. When $d_1 = d_2$, i.e., the air layers have equal thickness, the dispersion curves of the one-way SMPs connect at $k = 0$ due to symmetry, forming a single slow-wave peak. In addition, two total internal reflection (TIR) slow-wave peaks can arise in the YIG layer and the region between the

Optics EXPRESS

two metal boundaries if the structure is appropriately designed. To verify this conjecture, we first analyze the dispersion relations of the SMPs and TIR modes in the structure. First, note that a magnetized YIG (along the $-z$ direction) has a tensorial relative permeability given below:

$$\bar{\mu} = \begin{bmatrix} \mu_1 & -i\mu_2 & 0 \\ i\mu_2 & \mu_1 & 0 \\ 0 & 0 & 1 \end{bmatrix}, \text{with } \mu_1 = 1 + \frac{\omega_{\mathrm{m}}(\omega_0 - i\nu\omega)}{(\omega_0 - i\nu\omega)^2 - \omega^2},\ \mu_2 = \frac{\omega_{\mathrm{m}}\omega}{(\omega_0 - i\nu\omega)^2 - \omega^2} \tag{1}$$

The minus sign '-' of the off-diagonal element indicates and induces the nonreciprocal propagation characteristics of the guiding modes in magnetized YIG-based systems. ω_m and ω_0 represent the characteristic circular frequency and the precession angular frequency, respectively [39], and they are linearly related to the saturation magnetization of YIG and the EMF, respectively [40]. Note that ν represents the loss factor, and it has a relatively small impact on the nonreciprocal bands [41,42]. Thus, we ignore the loss effect in the theoretical analysis. For a SMP sustained at the air–YIG interface, the SMP exhibits exponential damping in both the air and YIG layers, with corresponding damping factors $\alpha_r = \sqrt{k^2 - \varepsilon_r k_0^2}$ (air) and $\alpha = \sqrt{k^2 - \varepsilon_m \mu_v k_0^2}$ (YIG). Considering the PEC boundaries along the y-direction of the structure, the dispersion relation of the SMP takes the following form:

$$\begin{cases} \left(\alpha^2 - A_1 A_2\right) \cdot \tanh(\alpha \cdot d_0) + (A_1 - A_2) \cdot \alpha = 0 \\ A_1 = \mu_v \alpha_r X_1 - \frac{\mu_2}{\mu_1} k,\ X_1 = \frac{1}{\tanh(\alpha_r d_2)} \\ A_2 = \mu_v \alpha_r X_2 - \frac{\mu_2}{\mu_1} k,\ X_2 = -\frac{1}{\tanh(\alpha_r d_1)} \end{cases} \tag{2}$$

When $d_1 = d_2$, we obtain $A_1 A_2 = \left(\frac{\mu_2}{\mu_1} k\right)^2 - \mu_v^2 \alpha_r^2 X_1^2$ and $A_1 - A_2 = 2\mu_v \alpha_r X_1$. In this case, it is easy to verify that Eq. (1) is symmetric with respect to $k = 0$. For TIR modes, the corresponding dispersion relations can be directly derived from Eq. (2) by replacing the damping factors (α_0 and α_r) with the oscillation factors $p_r = -i\alpha_r = \sqrt{\varepsilon_r k_0^2 - k^2}$ and $p = -i\alpha = \sqrt{\varepsilon_m \mu_v k_0^2 - k^2}$. Moreover, in the limit $k \to \pm\infty$, we have $\alpha \approx k$ and $\alpha_r \approx k$. As a result, Eq. (2) reduces to $\mu_1 + \mu_2 + 1 = 0$, yielding an asymptotic frequency (AF) of $\omega_{\mathrm{af}} = \omega_0 + 0.5\omega_m$ for the SMPs.

Figure 1(b) shows the complete dispersion curves of the SMPs and TIR modes. Note that deep-subwavelength-thick air and YIG layers, with $d_1 = d_2 = d_0 = 0.05\lambda_m$ ($\lambda_m = 2\pi c/\omega_{\mathrm{m}}$), are used to isolate clean first-order TIR modes and to engineer slow-wave peaks. As shown in Fig. 1(b), three slow-wave peaks—SW-1, SW-2, and SW-3—are successfully engineered in the structure. The red and green lines indicate the split dispersion branches of the SMPs, while the blue lines represent the TIR modes in YIG. Note that a traditional one-way MO waveguide [43] with a single air-YIG interface supports one-way SMPs due to broken time-reversal symmetry. In contrast, our design features two distinct air-YIG interfaces. As shown by the red and green curves in Fig. 1(b), this spatial symmetry ($d_1 = d_2$) leads to bidirectional modes with equal-magnitude but oppositely directed wave vectors below SW-2. Due to the sufficiently small longitudinal dimension of the structure, a clean first-order TIR dispersion curve with a slow-wave peak (SW-3) is observed in this case. Moreover, a bandgap exists between SW-1 and SW-2, which emerges only if the coupling between SMPs at the air–YIG interfaces is sufficiently strong, i.e., if d_0 is small enough. The dashed line shows a traditional one-way waveguide [43] consisting of a single air–YIG interface, where the YIG layer has a finite thickness ($d_0 = d_1 = 0.05\lambda_m$ in this case).

The dispersion relation for these one-way modes can be directly obtained from Eq. (2) by taking the limit $d_2 \to 0$, which leads to $A_1 \to \infty$. Under this condition, Eq. (2) simplifies to $-A_2 + \frac{\alpha}{\tanh(\alpha d_0)} = 0$. Substituting A_2 gives the final dispersion relation for one-way SMPs: $\frac{\mu_v \alpha_r}{\tanh(\alpha_r d_1)} + \frac{\mu_2}{\mu_1} k + \frac{\alpha}{\tanh(\alpha d_0)} = 0$. It is evident that SMPs can propagate unidirectionally within

Optics EXPRESS

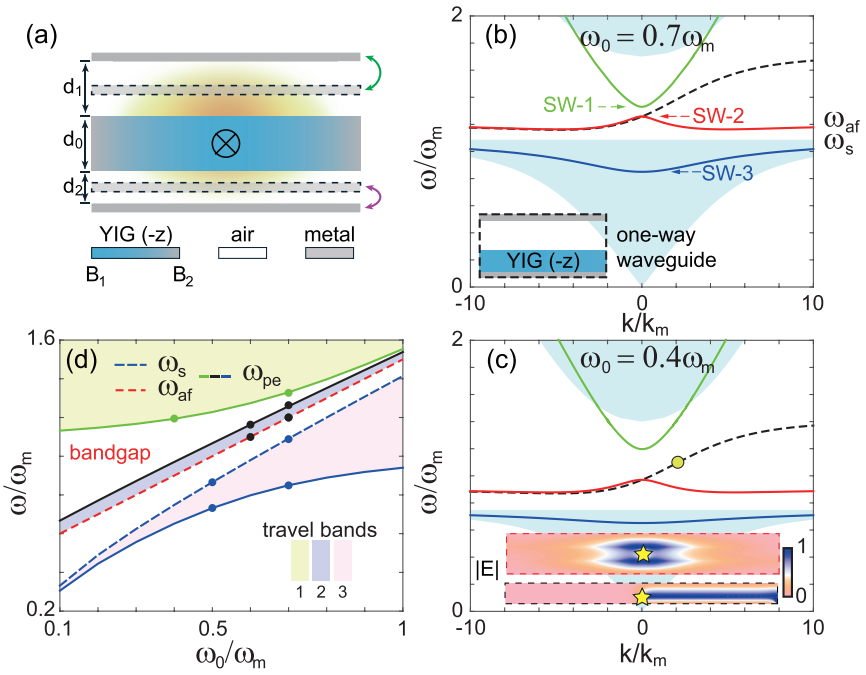

Fig. 1. Triple-band slow-wave dispersion in MO heterostructures. (a) Schematic of realizing triple-band slow-wave in a layered heterostructure. (b) Dispersion curves of SMPs in our structure (solid lines) and a typical one-way waveguide (dashed line) structure. The inset shows the schematic of the one-way waveguide. The thicknesses of the air and YIG layers are the same, $0.05\lambda_m$, for both cases. (c) The dispersion curves of the SMPs for $\omega_c = 0.4\omega_m$, while in (b), the value is $0.7\omega_m$. Inset: Electric field distributions from FEM simulations for (top) our proposed structure and (bottom) a reference one-way waveguide corresponding to the black dashed line. (d) The peak frequencies ω_{pe} (solid lines) of the three slow-wave peaks, ω_s (blue dashed line), and ω_{af} (red dashed line), are plotted as a function of the external magnetic field (ω_c). The other parameters are $\varepsilon_r = 1$ (air), $d_0 = d_1 = d_2 = 0.05\lambda_m$.

the aforementioned bandgap in this structure. Similarly, when the YIG layer is infinitely thick ($d_0 \to +\infty$), the green and red lines in Fig. 1(b) merge [44], and under this condition, both the bandgap between SW-1 and SW-2 and the slow-wave peaks disappear. As shown in Fig. 1(b), the slow-wave peak frequencies (ω_{pe}) of SW-1, SW-2, and SW-3 are approximately $1.33\omega_m$, $1.258\omega_m$, and $0.85\omega_m$, respectively. It is worth noting that SW-1 is very close to SW-2, which hampers the realization of rainbow trapping, as the target wave may easily slip into the adjacent dispersion branch.

Similar to topological photonic crystals [45,46], an effective way to enlarge the bandgap is by modifying the EMF. As shown in Fig. 1(c), the bandgap increases as the EMF decreases, with $\omega_0 = 0.4\omega_{\mathrm{m}}$. The inset illustrates the detailed wave propagation at $f = 1.3f_m$ (indicated by a circle in Fig. 1(c)). In the one-way waveguide (bottom panel), the wave propagates unidirectionally, as expected. In contrast, in our designed structure (top panel), the wave is confined at the two air–YIG interfaces due to strong coupling between the SMPs, which leads to the formation of a bandgap between SW-1 and SW-2. Fig. 1(d) shows how the EMF affects the dispersion diagram/curves of SMPs and TIR modes. As a result, all of the peak frequencies (solid lines)—ω_s ($= \sqrt{\omega_0(\omega_0 + \omega_m)}$, the resonant frequency of YIG) and ω_{af}—emerge as the EMF increases. The shaded areas represent the bidirectionally propagating SMPs and TIR modes, which contain the slow-wave peaks. It is clear that as the EMF increases, the highest SW-1 band gradually decreases,

Optics EXPRESS

while the lowest SW-3 band increases. Specifically, due to the nearly linear relationship between the two limits of the SW-2 band (the gray shaded area), the bandwidth of the middle SW-2 band remains almost unchanged. Moreover, the empty region between the black (ω_{pe2}) and green (ω_{pe1}) lines indicates the bandgap, and it is clear that the bandgap is much larger for smaller EMF values, which is consistent with the results shown in Figs. 1(b)-1(c). We note that the bandgap is related to ω_0, d_1 (d_2), and d_0, and we will further discuss its relationship with the thickness parameter later.

As shown in Fig. 1(d), the peak frequencies and travel bands are continuously tunable through the EMF, implying that waves with different operating frequencies can be trapped at different locations with carefully designed EMFs, i.e., rainbow trapping. Figure 2(a) shows our proposed straight heterostructure for bidirectional rainbow trapping, where the EMF is constant in the middle part, $B = B_1$ ($\omega_0 = \omega_{01}$), while for the other parts, the values of ω_0 are designed to change linearly from $\omega_0 = \omega_{01}$ to $\omega_0 = \omega_{02}$ (near the two ends). To trap the wave within the SW-1 band, the travel band of the middle part must be larger than that in the end part of the structure. Based on the results in Fig. 1(d), we choose a smaller EMF for the middle part to excite a broader band, while a larger EMF is chosen for the end part to prevent some of the excited waves from propagating through the structure. Specifically, we set $\omega_{01} = 0.4\omega_m$ and $\omega_{02} = 0.7\omega_m$. The left image of Fig. 2(b) shows the zoomed-in dispersion diagrams around the SW-1 band for $\omega_0 = 0.4\omega_m$ (dotted line) and $\omega_0 = 0.7\omega_m$. In the two side parts of the designed system, ω_0 gradually increases from $0.4\omega_m$ to $0.7\omega_m$, with the dispersion curves and ω_{pe1} increasing accordingly. Therefore, the waves within the green shaded area (chosen for simulations) in the left image of Fig. 2(b) cannot propagate through this device. Figure 2(b) presents the FEM simulation results for four different frequencies. As expected, clear rainbow trapping is observed, with the wave of higher frequency propagating longer and being trapped closer to the end. Similarly, we set $\omega_{01} = 0.7\omega_m$ and $\omega_{02} = 0.6\omega_m$ to trap waves within the SW-2 band. As shown in Fig. 2(c), a similar bidirectional rainbow trapping is observed, with the wave of higher frequency being trapped closer to the excitation point. For the SW-3 band, we set $\omega_{01} = 0.5\omega_m$ and $\omega_{02} = 0.7\omega_m$. Unlike the other two types of trapped rainbow, the electric field of the trapped wave in the SW-3 band is mostly confined to the YIG layer, while in the other cases, the wave propagates along the air-YIG interfaces.

Note that our proposed rainbow trapping is robust to manufacturing imperfections. As shown in the last images of Figs. 2(b)–2(d), two air holes with $r = 2$ mm were placed on the air-YIG interface to evaluate the impact of disorders on the rainbow trapping. The FEM simulation shows that the main difference between the perfect and imperfect cases is that the presence of disorders (e.g., air holes) in the structure causes the EM waves to reflect earlier. This could be used for advanced rainbow trapping or energy harvesting, which can be referred to as hierarchical trapping. We next investigate the robustness of the trapping location against disorder. Figure 3 investigates an extreme case in which air holes are centered in the YIG layer and extend beyond its thickness, i.e., $d_0 < 2r$. As shown in Fig. 3(a), the air holes are spaced 140 mm apart. In this imperfect heterostructure, the EM wave at $f = 1.28f_m$ near SW-1 remains trapped, as shown by simulations in the second panel of Fig. 3(a). The zoomed-in view shows that even under such an extreme condition, the EM wave can still couple into the guiding modes beyond the air holes. Moreover, most EM energy is clearly localized between the two air holes. Figure 3(b) shows the electric-field profile along the YIG center, revealing that the trapping zone, marked by two vertical lines, remains unchanged compared to the perfect case in Fig. 2(b). We conclude that, in most cases—particularly with small disorders-the trapping location in straight rainbow trapping is nearly unaffected by disorder unless it occurs precisely at the trapping site.

To the best of our knowledge, this is the first report of triple-band rainbow trapping, which has wide applications, including but not limited to highly efficient energy harvesting and storage. The next question is how to release the trapped rainbow or energy. One simple approach is to tune the

Optics EXPRESS

EMF. For example, set $\omega_0 = \omega_{01}$ for the entire structure. However, it is somewhat complex to flexibly and precisely adjust the EMF in practice. Here, we propose a novel method to achieve bidirectional rainbow trapping in this structure by changing the air or YIG thicknesses. To this end, we need to analyze the impact of d_1, d_2, and d_0 on the peak frequencies. For simplicity, we assume that the two air layers have equal thickness, i.e., $d_1 = d_2 = d_{1,2}$, throughout this paper, and compared to the equal condition ($d_1 = d_2$), the only key difference in the non-equal condition ($d_1 \neq d_2$) is that the slow-wave modes may shift left or right.

As demonstrated in Fig. 4(a), four different values of d_0 are chosen for the case where $d_{1,2} = 0.05\lambda_m$ and $\omega_0 = 0.4\omega_m$. Consequently, SW-1 (green line) and SW-3 (blue line) decrease as d_0 increases, leading to a decrease in ω_{pe1} and ω_{pe3}. In contrast, SW-2 slightly rises during the same process. Similarly, as shown in Fig. 4(b), for a heterostructure with consistent YIG, which is more feasible in our opinion, when $d_{1,2}$ increases from $0.03\lambda_m$ to $0.09\lambda_m$, interestingly,

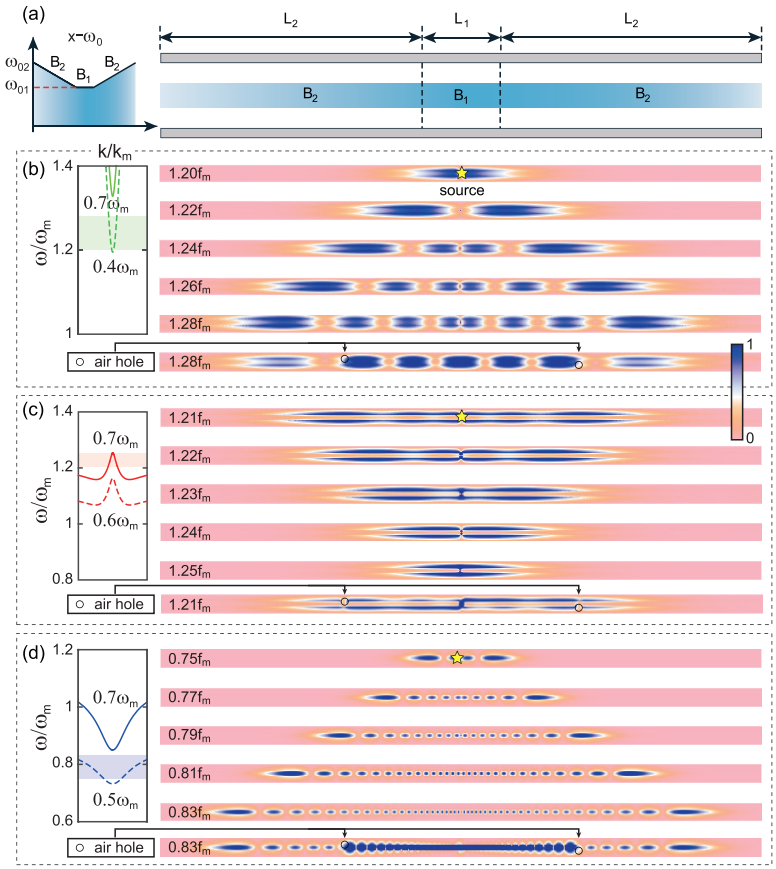

Fig. 2. Bidirectional rainbow trapping in straight waveguides. (a) The schematic of bidirectional rainbow trapping. The left picture denotes the EMF changes in the +x direction. Trapping of the (b) highest (SW-1), (c) middle (SW-2), and (d) lowest (SW-3) slow waves in a straight waveguide with linearly changing EMF, as shown in (a). The EMF (ω_0) at the two ends and the middle part are (b) $[0.7\omega_m, 0.4\omega_m]$, (c) $[0.6\omega_m, 0.7\omega_m]$, and (d) $[0.7\omega_m, 0.5\omega_m]$, respectively. The left panels of (b)-(d) demonstrate the zoomed-in pictures of the key dispersion curves of SMPs in each case. Two air holes (r = 2 mm) are introduced at the air-YIG interfaces to investigate the impact of disorder on bidirectional rainbow trapping, as shown in the final panels of (b–d). L_1 = 10 mm, L_2 = 175 mm, and ν = 0.001.

Optics EXPRESS

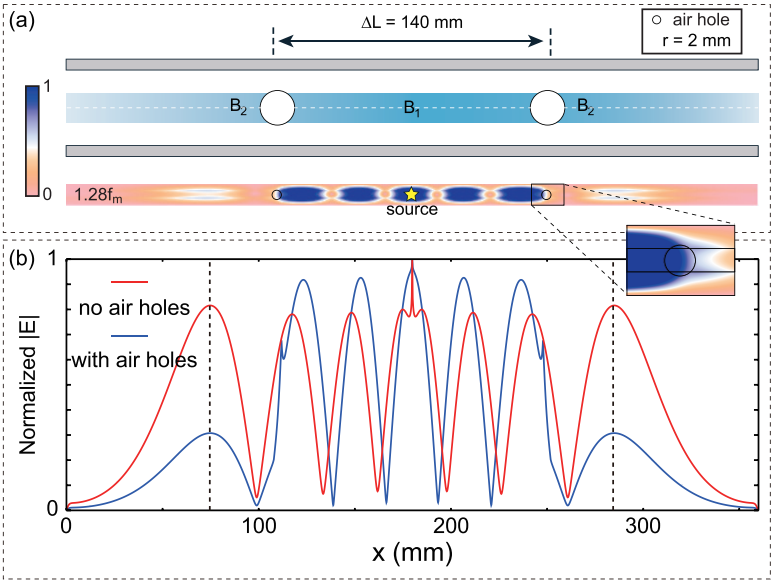

Fig. 3. Effect of structural disorder on triple-band rainbow trapping. (a) Top: Schematic of the straight MO heterostructure with two air holes (r = 2 mm) centered in the YIG layer. Bottom: Electric-field distribution near SW-1 at $f = 1.28f_m$ in the disordered structure. (b) Normalized electric-field profiles from FEM simulations for structures with (blue line) and without (red line) air holes, extracted along the white horizontal line in (a, top). Other parameters match those in Fig. 2(b).

all three slow-wave peaks decrease. Note that for both cases, the bandgap between SW-1 and SW-2 narrows as $d_{1,2}$ or d_0 increases (see the rightmost two images in Figs. 4(a) and 4(b)). Figures 4(c) and 4(d) provide more details for cases with varying d_0 and $d_{1,2}$. Our calculations show that with the monotonic increase of d_0 (see Fig. 4(c)) and $d_{1,2}$ (see Fig. 4(d)), the three peak frequencies exhibit monotonic changes. By applying the reverse concept of rainbow trapping used in Fig. 2, one can easily adjust, for example, the value of $d_{1,2}$ to make SW-1 and SW-3 decrease or make SW-2 increase, thereby allowing the trapped waves to be released as needed. Thus, the arrows in Figs. 4(c)-4(d) indicate the directions for releasing the trapped rainbow. Compared to single- and dual-band slow-wave systems, the key advantages of our structure are threefold: 1) a simpler configuration, 2) increased number of working bands enabling parallel computing and communication, and 3) enhanced and more versatile controllability. For instance, by increasing the air layer thickness, waves trapped near SW-1 can be released while those near SW-2 remain confined, thereby achieving selective manipulation of trapped electromagnetic waves across different frequency bands.

To verify the release theory proposed in Fig. 4, we performed several FEM simulations to demonstrate the release process for the three slow-wave peaks. We emphasize that in this paper, only the case of consistent d_0 was considered for releasing the trapped rainbow, as it is much easier in practice to adjust the air thicknesses rather than the YIG thickness. Figure 5(a) shows the schematic of rainbow trapping (left) and releasing (right) configurations. We aim to adjust $d_{1,2}$ by simply moving the metal layers and further control the trapping or releasing of EM waves. Figures 5(b)–5(d) demonstrate the FEM simulations for $d_0 = 0.05\lambda_m$, with the values of $d_{1,2}$ highlighted on the right of each image. As shown in Fig. 5(b), to release the trapped EM wave with $f = 1.20f_m$, we gradually increased $d_{1,2}$ according to the release direction marked in Fig. 4(d). As a result, as $d_{1,2}$ increases, the trapping area expands, and when $d_{1,2} = 0.08\lambda_m$, as shown in

Optics EXPRESS

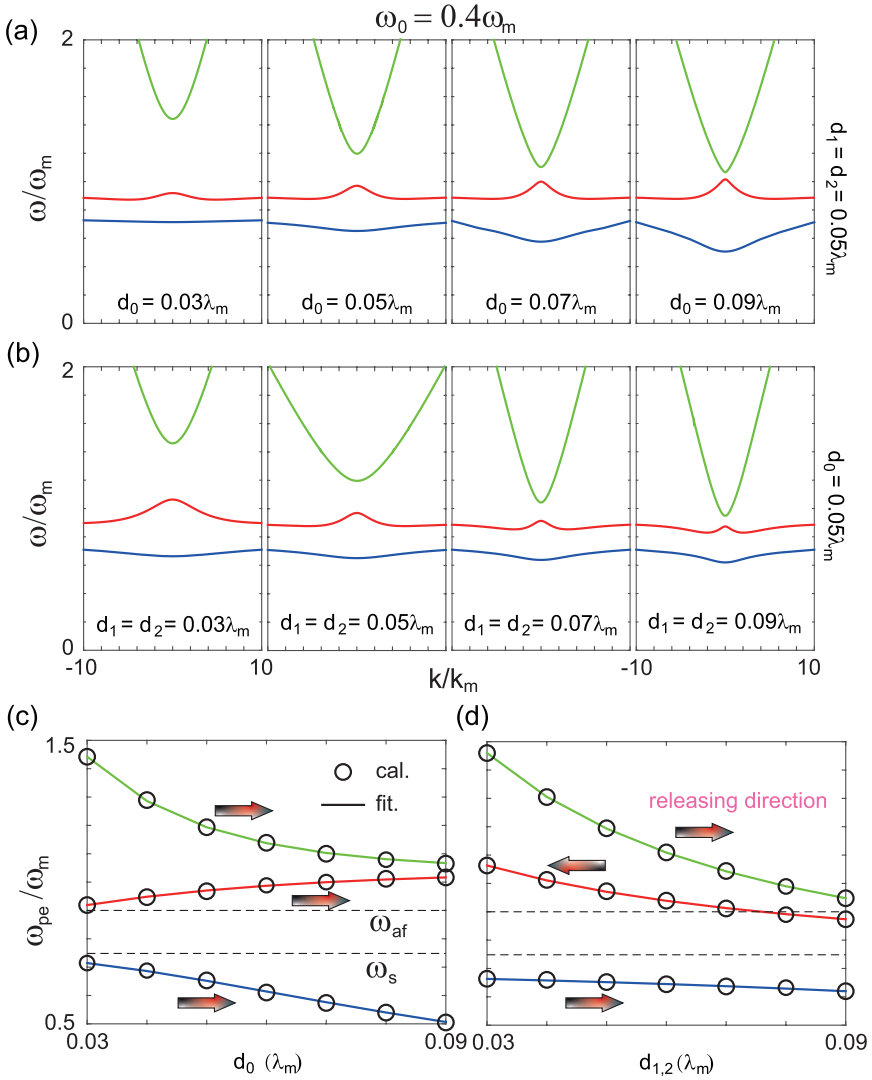

Fig. 4. Bidirectional rainbow trapping and releasing theory in straight configurations. Dispersion curves of SMPs around three slow-wave peaks when the waveguide has (a) constant and equal thickness of air layers ($d_1 = d_2 = d_{1,2}$, with $d_{1,2} = 0.05\lambda_m$) and different d_0 (YIG thickness), and (b) constant d_0 ($= 0.05\lambda_m$) and different air thicknesses ($d_1 = d_2 = d_{1,2}$). The peak frequencies (ω_{pe}) plotted as a function of (c) d_0 with fixed $d_{1,2} = 0.05\lambda_m$, and (d) $d_{1,2}$ with fixed $d_0 = 0.05\lambda_m$. The arrows indicate the direction in which one can manipulate to release the trapped waves, as shown in Fig. 2.

the last image of Fig. 5(b), the EM wave is finally released. To release the trapped EM waves in SW-2 and SW-3, we gradually decreased (as shown in Fig. 5(c)) and increased (as shown in Fig. 5(d)) $d_{1,2}$, respectively. As a result, the wave with $f = 1.25f_m$ within SW-2 is released when $d_{1,2} \approx 0.03\lambda_m$, and the wave with $f = 0.75f_m$ within SW-3 is released when $d_{1,2} \approx 0.09\lambda_m$. Thus, bidirectional rainbow trapping and releasing are achieved by adjusting the thickness parameters in the proposed heterostructure with gradual EMF.

Optics EXPRESS

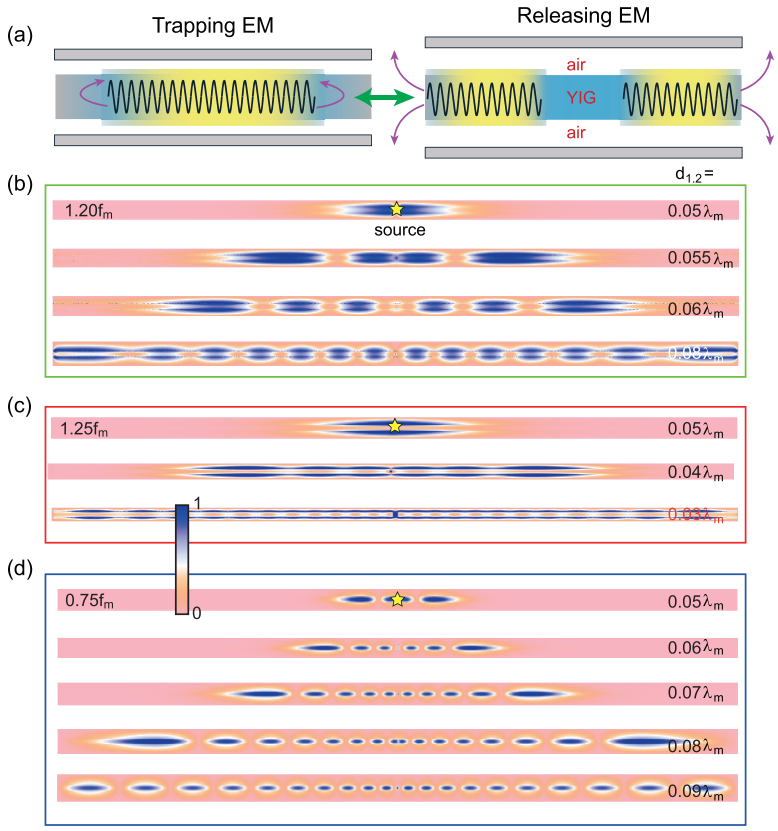

Fig. 5. Changing the air thicknesses to achieve bidirectional rainbow releasing in straight configurations. (a) Schematic of releasing the trapped rainbow by changing the air thicknesses. (b)-(d) Simulation verification of the release theory shown in (a) for (b) SW-1, (c) SW-2, and (d) SW-3, respectively. The EMF distributions in (b)-(d) are the same as in Fig. 2(b)–2(d). $d_0 = 0.05\lambda_m$, while the values of $d_{1,2}$ in the simulations are shown to the right of each picture. $\nu = 0.001$.

3. Tapered heterostructures for bidirectional RTR and dielectric sensing

Although RTR has been achieved in the aforementioned heterostructure with a varying EMF, it is also crucial to investigate RTR under a constant EMF. Figure 6(a) depicts one of our designed RTR structures, and as d_0 gradually increases ($d_{11}<d_{10}$) or decreases ($d_{11}>d_{10}$), slow-wave peaks should descend or rise accordingly. Figure 6(b) demonstrates the relation between the peak frequencies and d_0, as the total thickness ($d_0 + 2d_1$) of the structure is consistently $0.16\lambda_m$. Note that the EMF is consistent and that $\omega_0 = 0.4\omega_m$ in the structure. When d_0 increases from $0.03\lambda_m$ to $0.09\lambda_m$, SW-2 increases monotonically, SW-3 decreases monotonically, and SW-1 first decreases and then increases. We take SW-2 as an example to explain how EM trapping occurs. As discussed above, the EM wave within the region limited by ω_{af} and ω_{pe2} can always travel bidirectionally (as seen in the red shaded area in Fig. 6(b)). In contrast, any wave within the bandgap (the gray shaded area) cannot propagate at all. Thus, the EM wave with $f = f_m$ can be excited bidirectionally at the location with $d_0 = 0.08\lambda_m$ (marked by the red circle in Fig. 6(b)) in the tapered structure, and as d_0 decreases to $0.05\lambda_m$ (marked by the blue circle), it must be trapped somewhere between the two marked locations. More importantly, waves with different frequencies must be trapped at different locations in this tapered structure. Thus,

Optics EXPRESS

rainbow trapping can be achieved in a tapered structure with d_0 decreasing linearly from $0.08\lambda_m$ to $0.05\lambda_m$, as depicted by the left arrow. The corresponding trapping band in such a tapered heterostructure is $0.9537\omega_m<\omega<1.056\omega_m$. As shown in Fig. 6(c), the electric-field distribution in the simulations clearly shows standard rainbow trapping for four EM waves. To release the trapped waves, an obvious way is to enlarge d_0 for the whole structure, which can be achieved by inserting YIG wedges to make $d_0 = 0.08\lambda_m$ ($d_{1,2} = 0.04\lambda_m$). A simpler way to release the trapped waves is to decrease $d_{1,2}$ as shown in Fig. 5. According to our calculation, the trapped EM wave with $f = f_m$ can be released when the air thickness decreases by $0.025\lambda_m$, i.e., d_{10} decreases from $0.04\lambda_m$ to $0.015\lambda_m$. For the remaining two slow-wave peaks, one can design similar tapered heterostructures according to the d_0–ω_{pe} relation, as shown in Fig. 6(b), to achieve bidirectional RTR. Notably, experimental realization of RTR in the straight system is technically challenging due to the requirement of a linearly varying EMF, whereas the tapered RTR structure, as shown in Fig. 6, is easier to implement. The electromagnets can be tuned to provide a suitable constant EMF [47], and the primary challenge lies in fabricating high-quality YIG with a low loss factor, e.g., $\nu = 0.001$ or less.

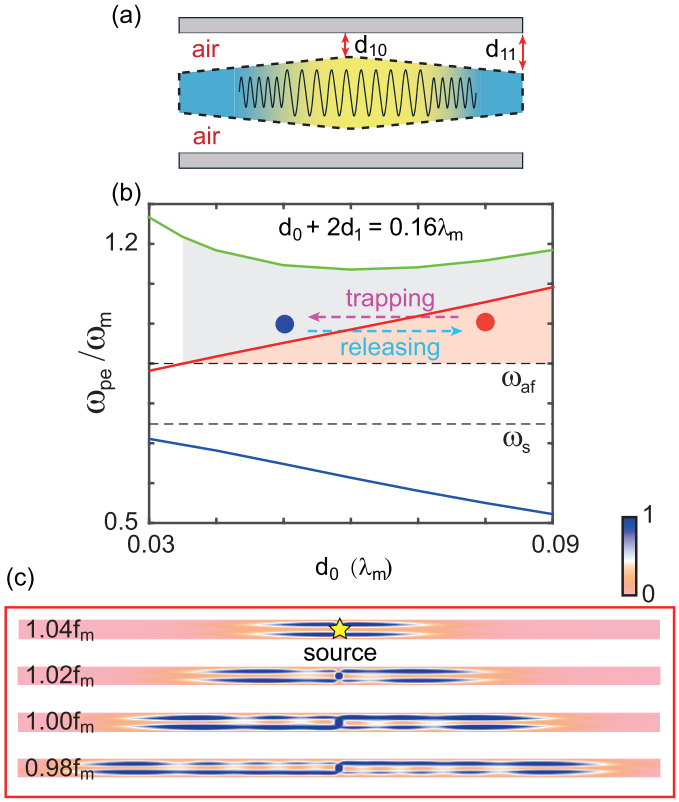

Fig. 6. Rainbow trapping and releasing in a tapered waveguide under a constant EMF. (a) Schematic of a tapered waveguide for rainbow trapping. (b) ω_{pe} as a function of d_0 in the tapered waveguide, where $d_0 + 2d_1 = 0.16\lambda_m$ ($d_1 = d_2$) and $\omega_0 = 0.4\omega_m$. (c) Electric-field distribution in simulations of the constant EMF-based rainbow trapping waveguide. $d_0 = 0.08\lambda_m$ (at the center) and $d_0 = 0.05\lambda_m$ (at the ends).

It is well known that the resonant or cut-off frequency of a dielectric-based waveguide is strongly influenced by its EM parameters, particularly the permittivity. Similarly, the triple-band slow-wave peaks in the MO heterostructure are expected to be sensitive to the dielectric properties.

Optics EXPRESS

Therefore, beyond enabling RTR, the MO heterostructure incorporating dielectrics also holds potential for other optical applications, such as dielectric detection or sensing. Figure 7(a) shows the schematic of our designed dielectric sensor, consisting of a uniform YIG layer, two tapered layers—air (right) and dielectric (left)—and PEC walls. We note that the right-side dielectric is set as air for comparison, but it can be replaced with other dielectrics as needed in practice. As demonstrated in Fig. 4(d), as $d_{1,2}$ (dielectric thickness) decreases, SW-1 shifts upward, and some guiding SMPs in the thicker configuration become trapped. As shown in Fig. 7(b), as $d_{1,2}$ decreases, the travel bands (regions above the solid lines) shrink in all cases. However, for a wave with $f = 1.3f_m$, the capture positions—defined by the intersection of the dashed line and the solid lines—differ depending on the dielectric permittivity ε_r. More specifically, as $d_{1,2}$ decreases, the horizontal dashed line intersects the solid curves for smaller ε_r values earlier, indicating that the $f = 1.3f_m$ wave will be trapped closer to the center in the tapered structure when the permittivity is lower.

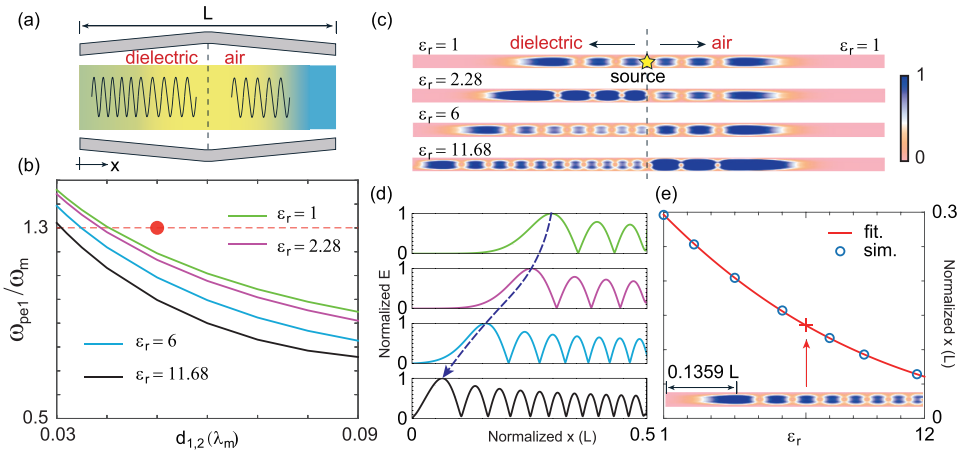

Fig. 7. Tapered heterostructure for dielectric sensing. (a) Schematic of a dielectric sensor based on triple-band slow-wave SMPs. (b) For dielectrics with varying permittivities, the peak frequencies (ω_{pe1}) of SW-1 in the tapered waveguide shown in (a) are plotted as a function of d_1 with $d_0 = 0.05\lambda_m$. (c) Electric-field distributions in simulations with different left-side dielectrics. (d) Normalized electric fields in the left region of the waveguide from the simulations in (c). (e) Predicted normalized trapping position x as a function of the dielectric permittivity. The inset shows simulation results for a dielectric with $\varepsilon_r = 7$. Blue circles indicate the trapping positions based on our FEM simulations.

To verify our analysis, we conducted FEM simulations using different dielectric materials. As shown in Fig. 7(c), four different relative permittivities (ε_r) were chosen for the left dielectric, while the right dielectric was set as air ($\varepsilon_r = 1$). As a result, the wave ($f = 1.3f_m$) is trapped in all cases, consistent with our analysis. The capture positions differ across materials, and the smallest trapping region occurs when $\varepsilon_r = 1$. Figure 7(d) provides further details about the trapped waves in the left section. As indicated by the arrow, the capture position gradually shifts toward the left end of the waveguide. Based on this observation, the permittivity of the left and right dielectrics can be compared by identifying their respective trapping distances within the structure. Furthermore, by plotting the relationship between dielectric permittivity and capture position—either experimentally or through simulations—the permittivity of unknown materials can be inferred. As shown in Fig. 7(e), the blue circles represent capture positions corresponding to different ε_r values obtained from FEM simulations of the proposed

Optics EXPRESS

heterostructure. The red line represents a polynomial fit to the simulation data, given by $x = -2.28253 \times 10^{-5}\varepsilon_r^3 + 0.0015403\varepsilon_r^2 - 0.037872\varepsilon_r + 0.33283$.

To validate the fitting curve, we simulated the case $\varepsilon_r = 7$ (see inset of Fig. 7(e)). The resulting capture position was $x \approx 0.1359$ L, compared to 0.1354 L from the fitted curve. The relative error is approximately 0.37%, confirming the high sensitivity of our proposed dielectric sensor. We emphasize that similar dielectric sensors based on SW-2 and/or SW-3 can be designed using the same method demonstrated in Fig. 7. It is also worth emphasizing that in practical implementations, the fitting function should be adapted/modified according to the specific characteristics of the target device. In theory, disorder or imperfection may distort the fitting curve and thus affect the sensitivity or precision of the proposed dielectric sensor. However, as discussed in Fig. 3, the trapping location remains nearly unchanged even under significant disorder, provided it does not occur exactly at the trapping site. Therefore, the effect of disorder can be safely neglected in most practical scenarios.

4. Conclusion

In conclusion, we have proposed a specialized MO heterostructure composed of metal, dielectric (e.g., air), and magnetized YIG to engineer unique dispersion relations featuring triple-band slow-wave peaks, labeled SW-1, SW-2, and SW-3. Moreover, triple-band RTRs in both straight and tapered heterostructures have been achieved by using linearly varying and constant EMFs, respectively. In the straight heterostructure, the slow-wave peak frequencies shift under the influence of the EMF. By carefully designing the EMFs at the center and boundaries of the structure, rainbow trapping is achieved across three distinct slow-wave bands. To release the trapped EM waves, we have proposed a simple and practical approach: tuning the air-layer thickness, or equivalently, moving the metal layer. FEM simulations under lossy conditions clearly demonstrate bidirectional RTR in the straight heterostructure. For practical applications, using a constant EMF is more suitable. Accordingly, a tapered heterostructure was designed to realize bidirectional RTR. Taking SW-2 as an example, we have further designed a customized heterostructure featuring a thick central YIG region and tapered YIG sides. Bidirectional RTR was confirmed through theoretical analysis and numerical simulations. Building on this, we have proposed a high-performance sensor for detecting dielectric permittivity. By identifying the capture position of the trapped EM waves, the relative permittivity of the dielectric can be determined with high precision. Our analysis indicates that the relative detection error can be as low as 0.37%. Notably, in simulations, this relative error is directly influenced by the grid resolution; therefore, it can be further reduced with higher simulation precision. In practical applications, the device sensitivity may depend on the precision of auxiliary detection equipment. The proposed bidirectional RTR heterostructures, together with the dielectric sensor, hold significant promise for applications in areas such as energy storage, information buffering, and biosensing. Based on the theoretical framework developed in this work, multi-band slow-wave propagation and RTR can also be realized using other MO materials in different frequency regimes.

Funding. National Natural Science Foundation of China (12404143, 62101496); Program of Luzhou Science and Technology Bureau (2023JYJ046, 2023JYJ032); Project of the Central Government in Guidance of Local Science and Technology Development (2024ZYD0270).

Disclosures. The authors declare that there are no conflicts of interest related to this article.

Data availability. No data were generated or analyzed in the presented research.

References

1. T. F. Krauss, "Why do we need slow light?" Nat. Photonics **2**(8), 448–450 (2008).
2. Y. A. Vlasov, M. O'boyle, H. F. Hamann, *et al.*, "Active control of slow light on a chip with photonic crystal waveguides," Nature **438**(7064), 65–69 (2005).

Optics EXPRESS

3. G. Arregui, J. Gomis-Bresco, C. M. Sotomayor-Torres, *et al.*, "Quantifying the robustness of topological slow light," Phys. Rev. Lett. **126**(2), 027403 (2021).
4. L. V. Hau, S. E. Harris, Z. Dutton, *et al.*, "Light speed reduction to 17 metres per second in an ultracold atomic gas," Nature **397**(6720), 594–598 (1999).
5. J. Duan, L. Chen, Y. Gao, *et al.*, "Tunable electromagnetic-induced transparent metasurfaces and their sensing effects," Opt. Laser Technol. **183**, 112326 (2025).
6. R. Liu, T. Liu, Y. Wang, *et al.*, "Slowing down the speed of light using an electromagnetically-induced-transparency mechanism in a modified reservoir," Phys. Rev. A **96**(5), 053823 (2017).
7. B. Zhang, A. Dong, J. Wang, *et al.*, "Strong coupling and electromagnetically induced transparency in multiple-BIC-driven metasurfaces," Nano Lett. **25**(11), 4568–4575 (2025).
8. T. Baba, "Slow light in photonic crystals," Nat. Photonics **2**(8), 465–473 (2008).
9. K. L. Tsakmakidis, A. D. Boardman, and O. Hess, "?trapped rainbow? storage of light in metamaterials," Nature **450**(7168), 397–401 (2007).
10. E. Di Gennaro, P. Parimi, W. Lu, *et al.*, "Slow microwaves in left-handed materials," Phys. Rev. B **72**(3), 033110 (2005).
11. J. Xu, C. Zhong, S. Zhuang, *et al.*, "Slow-wave hybrid magnonics," Phys. Rev. Lett. **132**(11), 116701 (2024).
12. C. Wu, A. B. Khanikaev, and G. Shvets, "Broadband slow light metamaterial based on a double-continuum fano resonance," Phys. Rev. Lett. **106**(10), 107403 (2011).
13. M. J. Akram, F. Ghafoor, M. M. Khan, *et al.*, "Control of fano resonances and slow light using bose-einstein condensates in a nanocavity," Phys. Rev. A **95**(2), 023810 (2017).
14. K. Kuruma, H. Yoshimi, Y. Ota, *et al.*, "Topologically-protected single-photon sources with topological slow light photonic crystal waveguides," Laser Photonics Rev. **16**(8), 2200077 (2022).
15. C. Murendranath Patil, G. Arregui, M. Mechlenborg, *et al.*, "Observation of slow light in glide-symmetric photonic-crystal waveguides," Opt. Express **30**(8), 12565–12575 (2022).
16. H. Yoshimi, T. Yamaguchi, Y. Ota, *et al.*, "Slow light waveguides in topological valley photonic crystals," Opt. Lett. **45**(9), 2648 (2020).
17. A. Figotin and I. Vitebskiy, "Slow wave phenomena in photonic crystals," Laser Photonics Rev. **5**(2), 201–213 (2011).
18. H. Yoshimi, T. Yamaguchi, R. Katsumi, *et al.*, "Experimental demonstration of topological slow light waveguides in valley photonic crystals," Opt. Express **29**(9), 13441–13450 (2021).
19. F. Wang, J. S. Jensen, and O. Sigmund, "Robust topology optimization of photonic crystal waveguides with tailored dispersion properties," J. Opt. Soc. Am. B **28**(3), 387–397 (2011).
20. M. Shinkawa, N. Ishikura, Y. Hama, *et al.*, "Nonlinear enhancement in photonic crystal slow light waveguides fabricated using CMOS-compatible process," Opt. Express **19**(22), 22208–22218 (2011).
21. H. Wen, M. Terrel, S. Fan, *et al.*, "Sensing with slow light in fiber bragg gratings," IEEE Sens. J. **12**(1), 156–163 (2012).
22. L. Liang, X. Zhou, J.-H. Hu, *et al.*, "Rainbow trapping based on higher-order topological corner modes," Opt. Lett. **47**(6), 1454–1457 (2022).
23. K. Dixon, A. O. Montazeri, M. Shayegannia, *et al.*, "Tunable rainbow light trapping in ultrathin resonator arrays," Light: Sci. Appl. **9**(1), 194 (2020).
24. W. Zhao, Y. Zheng, and C. Lu, "Topological rainbow trapping based on non-hermitian twisted piecing photonic crystals," Photonics Res. **10**(12), 2728–2733 (2022).
25. S. Fang, Z. Yang, Y. Tao, *et al.*, "Design and experimental realization of triple-band filtering metamaterial in sub-terahertz band enabled by conductivity coupling response of two identical split rings," Opt. Laser Technol. **183**, 112345 (2025).
26. B.-X. Wang, G. Duan, W. Lv, *et al.*, "Design and experimental realization of triple-band electromagnetically induced transparency terahertz metamaterials employing two big-bright modes for sensing applications," Nanoscale **15**(45), 18435–18446 (2023).
27. Q. Yang, H. Xiong, J.-H. Deng, *et al.*, "Polarization-insensitive composite gradient-index metasurface array for microwave power reception," Appl. Phys. Lett. **122**(25), 253901 (2023).
28. H. Xiong, Q. Yang, Y.-Z. Huang, *et al.*, "A high-efficiency hybrid microwave power receiving metasurface array with dual matching of surface impedance and phase gradient," Appl. Phys. Lett. **125**(4), 043901 (2024).
29. H. Xiong, Q. Yang, Y.-Z. Huang, *et al.*, "High-efficiency microwave wireless power transmission via reflective phase gradient metasurfaces and surface wave aggregation," ACS Appl. Mater. Interfaces **16**(44), 60189–60196 (2024).
30. H. Xiong, J.-Y. Xie, Y.-J. Liu, *et al.*, "Microwave hyperthermia technology based on near-field focused metasurfaces: Design and implementation," Adv. Funct. Mater. **35**(1), 2411842 (2025).
31. H. Hu, D. Ji, X. Zeng, *et al.*, "Rainbow trapping in hyperbolic metamaterial waveguide," Sci. Rep. **3**(1), 1249 (2013).
32. J. Li, G. Hu, L. Shi, *et al.*, "Full-color enhanced second harmonic generation using rainbow trapping in ultrathin hyperbolic metamaterials," Nat. Commun. **12**(1), 6425 (2021).
33. J. Xu, Y. Luo, K. Yong, *et al.*, "Topological and high-performance nonreciprocal extraordinary optical transmission from a guided mode to free-space radiation," Commun. Phys. **6**(1), 339 (2023).
34. K. L. Tsakmakidis, L. Shen, S. A. Schulz, *et al.*, "Breaking lorentz reciprocity to overcome the time-bandwidth limit in physics and engineering," Science **356**(6344), 1260–1264 (2017).

Optics EXPRESS

35. J. Xu, S. Xiao, P. He, *et al.*, "Realization of broadband truly rainbow trapping in gradient-index metamaterials," Opt. Express **30**(3), 3941–3953 (2022).
36. J. Xu, P. He, D. Feng, *et al.*, "Slow wave and truly rainbow trapping in a one-way terahertz waveguide," Opt. Express **29**(7), 11328–11341 (2021).
37. A. Serga, A. Chumak, and B. Hillebrands, "Yig magnonics," J. Phys. D: Appl. Phys. **43**(26), 264002 (2010).
38. R.-Y. Zhang, X. Cui, Y.-S. Zeng, *et al.*, "Bulk–spatiotemporal vortex correspondence in gyromagnetic zero-index media," Nature **641**(8065), 1142–1148 (2025).
39. D. M. Pozar, *Microwave Engineering* (John wiley & sons, 2011).
40. G.-G. Liu, Z. Gao, Q. Wang, *et al.*, "Topological Chern vectors in three-dimensional photonic crystals," Nature **609**(7929), 925–930 (2022).
41. Q. Shen, J. Yan, and X. Zheng, "Ultrawideband unidirectional surface magnetoplasmons based on remanence for the microwave region," Opt. Mater. Express **11**(7), 2335–2347 (2021).
42. Z. Wang, Y. Chong, J. D. Joannopoulos, *et al.*, "Reflection-free one-way edge modes in a gyromagnetic photonic crystal," Phys. Rev. Lett. **100**(1), 013905 (2008).
43. P. He, Y. Shen, S. Xiao, *et al.*, "Precisely tunable and predictable index-near-zero modes across continuous and broad bands," Appl. Phys. Lett. **124**(16), 161109 (2024).
44. Q. Shen, Y. You, J. Xu, *et al.*, "Mechanically scanned leaky-wave antenna based on a topological one-way waveguide," Front. Phys. **15**(3), 33601 (2020).
45. Y. Wang, H.-X. Wang, L. Liang, *et al.*, "Hybrid topological photonic crystals," Nat. Commun. **14**(1), 4457 (2023).
46. T. Liu, N. Kobayashi, K. Ikeda, *et al.*, "Topological band gaps enlarged in epsilon-near-zero magneto-optical photonic crystals," ACS Photonics **9**(5), 1621–1626 (2022).
47. S. Li, K. L. Tsakmakidis, T. Jiang, *et al.*, "Unidirectional guided-wave-driven metasurfaces for arbitrary wavefront control," Nat. Commun. **15**(1), 5992 (2024).